Supplementary Information (SI) for Journal of Materials Chemistry A.
This journal is © The Royal Society of Chemistry 2026

Supporting Information

Spectroscopy evidence for directional oxygen ionic transport in correlated oxide heterostructures with tunable migration dynamics

*Xuanchi Zhou [1, 2 *], Xiaohui Yao [1], Xiaomei Qiao [1]*

[1] *Key Laboratory of Magnetic Molecules and Magnetic Information Materials of Ministry of Education & School of Materials Science and Engineering, Shanxi Normal University, Taiyuan, 030031, China*

[2] *Research Institute of Materials Science, Shanxi Key Laboratory of Advanced Magnetic Materials and Devices, Shanxi Normal University, Taiyuan 030031, China*

*Authors to whom correspondence should be addressed: *xuanchizhou@sxnu.edu.cn* *(X. Zhou)*.

This file includes:

Supplementary Figures 1-14, Supplementary Table 1 and Supplementary References.

Contents

Figure S1. Comparison of thermal annealing and chemical potential gradient for engineering oxygen vacancies.

Figure S2. HRTEM image for VO_2/Al_2O_3 (0001) heterostructure.

Figure S3. Surface morphology and thickness of VO_2 film deposited on Al_2O_3 substrate using AFM technique.

Figure S4. AFM images for the VO_2/Al_2O_3 heterostructure with and without the TiO_2 overlayer.

Figure S5. Comparison of the TiO_2/VO_2 system fabricated under oxygen-rich conditions.

Figure S6. The ρ-T curves for bare TiO_2 film deposited on *c*-plane Al_2O_3 substrate.

Figure S7. Comparing the ρ-T curves for VO_2 films through vacuum annealing and $\Delta\mu_O$-driven oxygen ionic transport.

Figure S8. The ρ-T curves for $TiO_2/VO_2/Al_2O_3$ heterostructure through oxidative annealing.

Figure S9. Repeatability experiment for $\Delta\mu_O$-induced oxygen ionic transport.

Figure S10. XRD patterns compared for the VO_2/Al_2O_3 heterostructure with and without TiO_2 overlayer.

Figure S11. sXAS spectra of TiO_2/VO_2 system with an ultrathin TiO_2 overlayer.

Figure S12. XPS survey and Ti 2*p* spectra of TiO_2/VO_2 system.

Figure S13. O-*K* edge sXAS spectra compared for TiO_2 overlayer deposited under different oxygen pressures.

Figure S14. O-*K* edge sXAS spectrum of the grown VO_2 film on *m*-plane Al_2O_3 substrate.

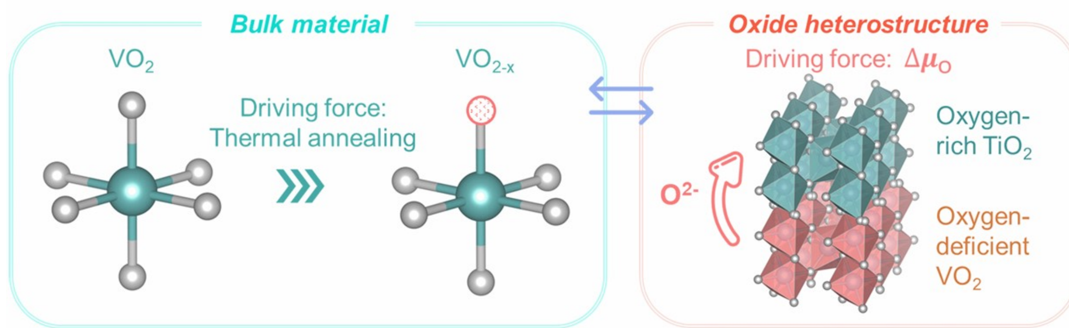

Supplementary Figure 1. Schematic of thermal annealing and chemical potential gradient strategies for introducing oxygen vacancies in oxide materials. In single bulk material, thermal annealing in an oxygen-deficient atmosphere is commonly employed to introduce abundant oxygen vacancies.[1, 2] Beyond that, the built-in oxygen chemical potential gradient ($\Delta\mu_O$) across the TiO_2/VO_2 system introduces an innovative strategy to spontaneously drive the unidirectional oxygen ionic transport in oxide heterostructures.[3-5] This $\Delta\mu_O$ gradient drives controllable oxygen ionic migration across the oxide heterointerface from underlying VO_2 layer to TiO_2 overlayer, giving rise to oxygen-deficient states in VO_2 and oxygen-enriched states in TiO_2.

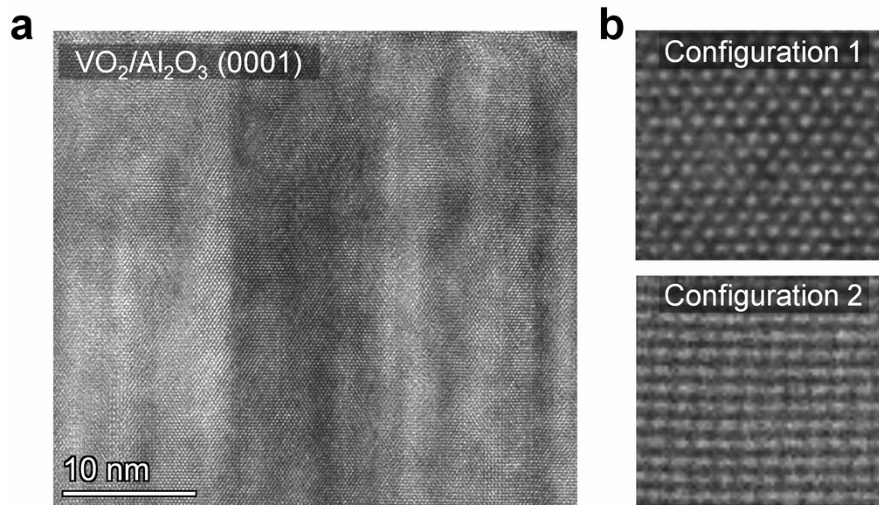

Supplementary Figure 2. a, Cross-sectional high-resolution transmission electron microscopy (HRTEM) image of the as-grown VO_2 film on an Al_2O_3 (0001) substrate. **b,** Two distinct atomic configurations in the VO_2 lattice deposited on the *c*-plane Al_2O_3 template, forming a vertically aligned domain boundaries within the heterostructure. The symmetry mismatch and β angular deviation between the rutile VO_2 film and the hexagonal Al_2O_3 substrate lead to the formation of possibly existed twin variants, in turn, resulting in a vertically aligned domain boundary structure.[6, 7]

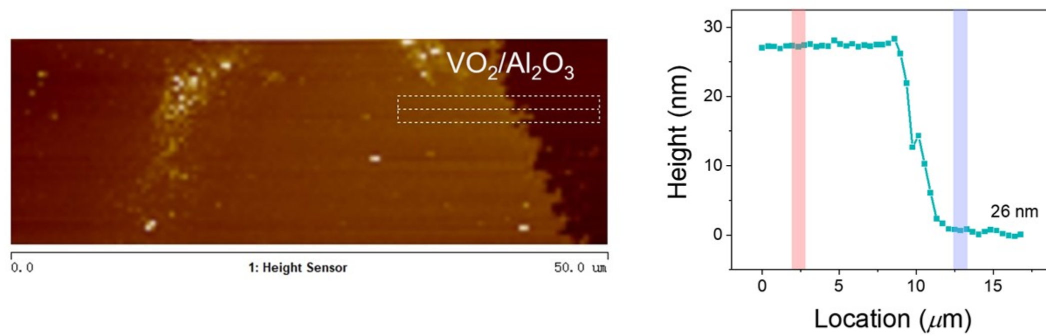

Supplementary Figure 3. Atomic force microscopy (AFM) topography images for the as-grown VO_2/Al_2O_3 (0001) heterostructure. It is found that the thickness for the underlying VO_2 film in TiO_2/VO_2 system is estimated to be around 26 nm via using AFM techniques.

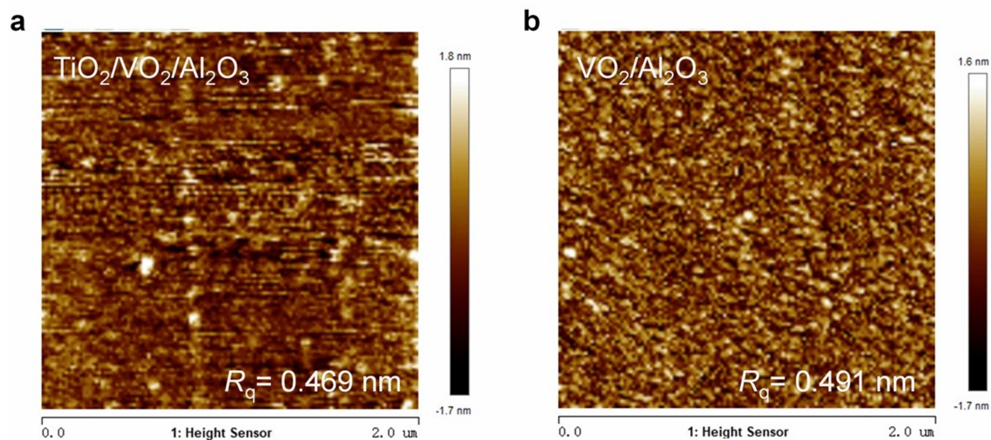

Supplementary Figure 4. Atomic force microscope (AFM) images for **a,** $TiO_2/VO_2/Al_2O_3$ heterostructure and **b**, VO_2/Al_2O_3 heterostructure. The atomically smooth film surfaces of as-grown TiO_2/VO_2 heterostructure are identified by using AFM technique, with a root-mean-square roughness (R_q) on the order of 0.5 nm being identified. The R_q value of heterostructure surface is not pronouncedly altered via the introduction of TiO_2 overlayer.

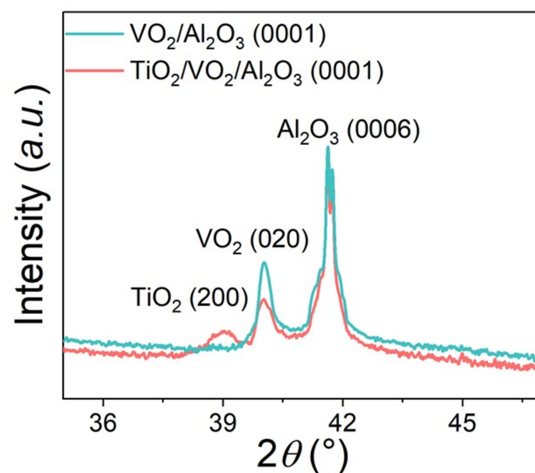

Supplementary Figure 5. X-ray diffraction (XRD) patterns for $TiO_2/VO_2/Al_2O_3$ heterostructures with the deposition of TiO_2 overlayer at 600 °C and 5 Pa. Depositing the TiO_2 overlayer under an oxygen-rich conditions leads to the formation of crystalline TiO_2, as evidenced by the characteristic diffraction peaks associated with the (002) plane of TiO_2. This observation starkly differs from an amorphous TiO_2 overlayer under mild growth conditions (e.g., 250 °C, 1 Pa), without the Bragg reflections being detected.

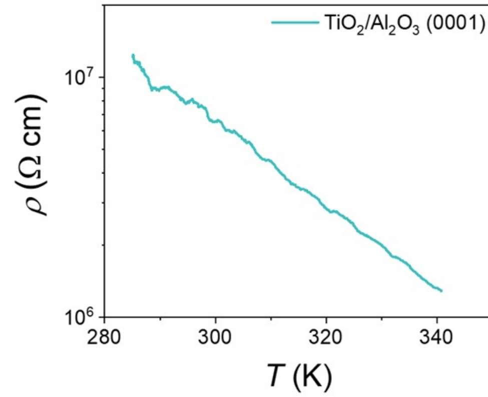

Supplementary Figure 6. The ρ-T curves for bare TiO_2 film deposited on c-plane Al_2O_3 substrate. The top TiO_2 overlayer was found to be insulating, and the Al_2O_3 substrate was also highly insulating. Therefore, the electrical transport properties of the $TiO_2/VO_2/Al_2O_3$ heterostructure were determined to originate mainly from the VO_2 layer.

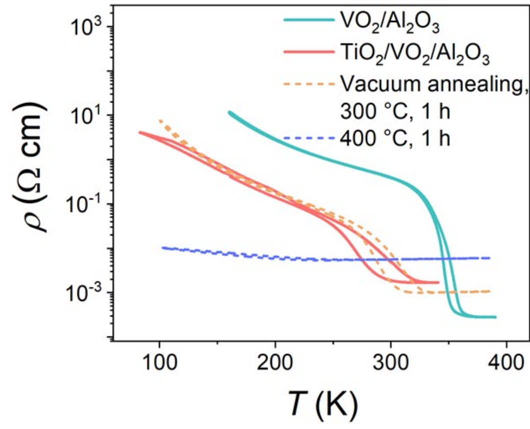

Supplementary Figure 7. Comparing the ρ-T curves for VO_2 films through vacuum annealing and $\Delta\mu_O$-driven oxygen ionic transport. When vacuum-annealed VO_2 films were compared with $\Delta\mu_O$-driven TiO_2/VO_2 samples, it was found that although complete metallization is achievable through extensive vacuum annealing, $\Delta\mu_O$-driven oxygen ionic transport proves more effective than a milder vacuum annealing treatment, providing a more controllable pathway.

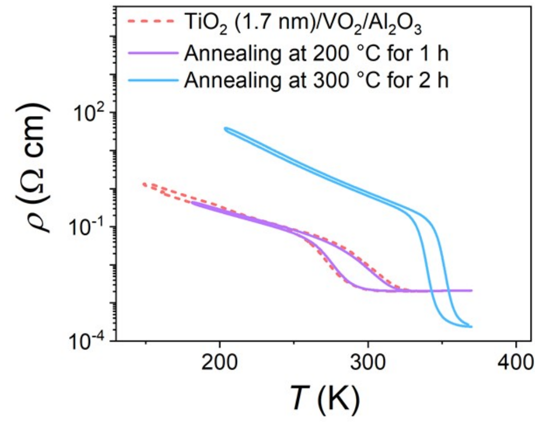

Supplementary Figure 8. The ρ-T curves for $TiO_2/VO_2/Al_2O_3$ heterostructure through oxidative annealing. Upon oxidative annealing at 300 ºC for 2 h under ambient atmosphere, the defect-driven depression of the IMT functionality in VO_2 reversibly transits toward the pristine state, exhibiting a T_{IMT} similar to that of stoichiometric VO_2.

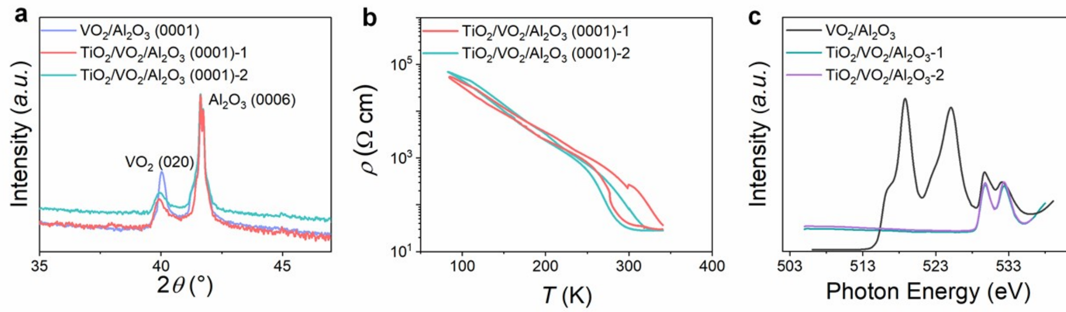

Supplementary Figure 9. a, X-ray diffraction (XRD) patterns **b,** temperature dependence of material resistivity (ρ-T) curves and **c,** soft X-ray absorption spectroscopy (sXAS) spectra compared for underlying VO_2 layer with and without TiO_2 overlayer. Analogous to the findings shown in the main text, oxygen deficiency in underlying VO_2 layer through directional oxygen ionic transport results in the lattice expansion and carrier delocalization. Furthermore, defect-associated band-filling control over the electronic band structure of VO_2 is demonstrated by the reduced t_{2g}/e_g peak intensity ratio in their O-K edge sXAS spectra.[8-11]

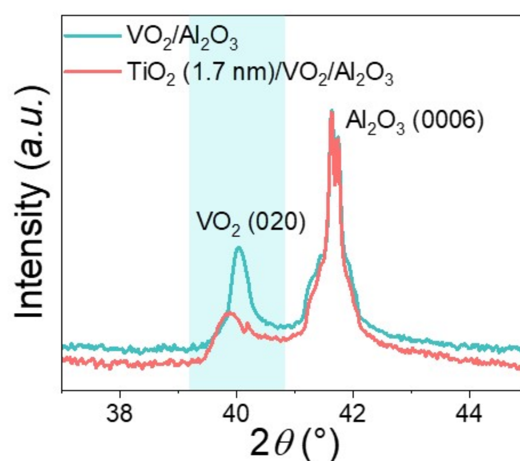

Supplementary Figure 10. XRD patterns compared for the VO_2/Al_2O_3 heterostructure with and without a 1.7 nm-thick TiO_2 overlayer. Similar to the TiO_2 (13 nm)/VO_2/Al_2O_3 heterojunction, the introduction of an ultra-thin 1.7 nm TiO_2 overlayer induces oxygen ion migration driven by the chemical potential difference between the underlying VO_2 and the intermediate TiO_2 layer. This process leads to the formation of an oxygen-deficient VO_{2-x} phase in the bottom VO_2 layer, accompanied by corresponding lattice expansion.

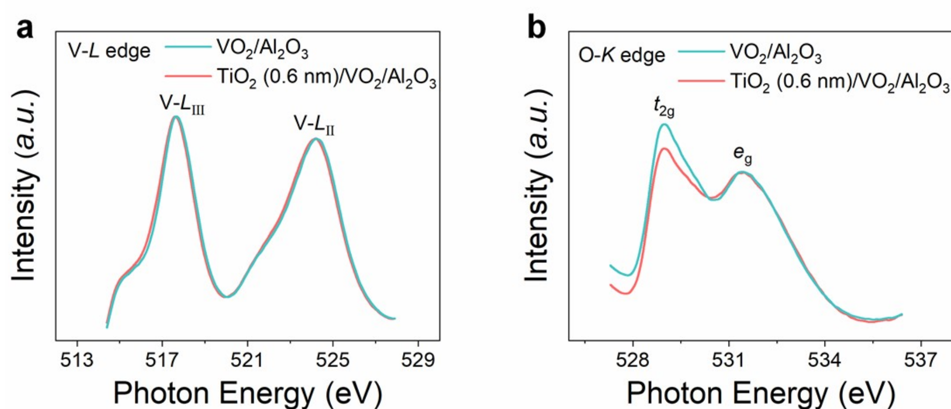

Supplementary Figure 11. The **a,** V-*L* edge and **b** O-*K* edge of sXAS spectra compared for the VO_2/Al_2O_3 heterostructure with and without the 0.6 nm-thick TiO_2 overlayer. By depositing an ultrathin TiO_2 overlayer on VO_2 thin films, the electron occupancy in the t_{2g} orbital is evident by a reduced t_{2g}/e_g peak intensity ratio in their O-*K* edge sXAS spectra. In contrast, no pronounced spectral shift is detected at the V-*L* edge for VO_2 after capped with the TiO_2 overlayer, likely attributable to an insufficient thickness of the TiO_2 capping layer.

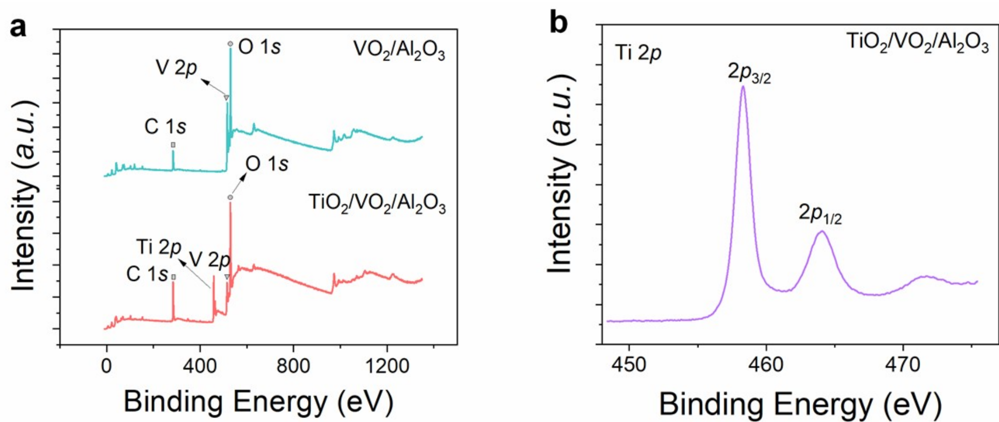

Supplementary Figure 12. a, Comparative XPS survey spectra of VO_2/Al_2O_3 heterostructures with and without TiO_2 capping layer. **b,** Ti 2*p* energy level of XPS spectrum for the $TiO_2/VO_2/Al_2O_3$ heterostructure. It is noteworthy that the characteristic Ti 2*p* peaks observed for the $TiO_2/VO_2/Al_2O_3$ heterostructure identify the presence of TiO_2 overlayer, contrasting sharply with the absent Ti 2*p* signal in VO_2/Al_2O_3 hybrid.

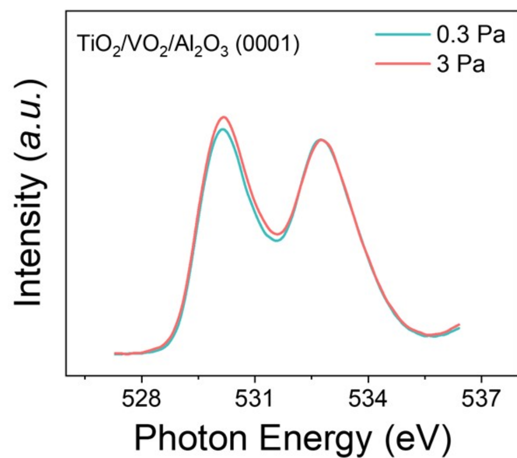

Supplementary Figure 13. The sXAS spectra compared for the underlying VO_2 layer capped with TiO_2 overlayers deposited at different oxygen pressures. A lower P_{o_2} used during TiO_2 growth tends to render a more pronounced the reduction in the intensity ratio of the t_{2g} peak to the e_g peak of underlying VO_2. This systematic decrease in the t_{2g}/e_g ratio indicates an enhanced electron filling in the low-energy t_{2g} orbitals of VO_2, which is attributed to an increased oxygen vacancy concentration in the VO_2 lattice via an accelerated oxygen ionic dynamics.

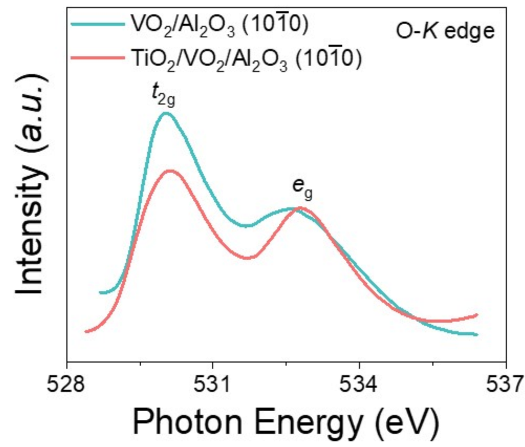

Supplementary Figure 14. The O-*K* edge of sXAS spectra of VO_2 film deposited on the *m*-plane Al_2O_3 substrates. Oxygen deficiency in underlying VO_2 layer through directional oxygen ionic transport is demonstrated by a decreased t_{2g}/e_g ratio in its O-*K* edge spectra, owing to the defect-related electron doping. These findings indicate that whether vertically nor inclined domain boundary configuration in the lattice can offer an efficient pathway for oxygen ionic diffusion, differing from the horizontally aligned ones.

Table S1 The ratio of the peak area and FWHM of the first peak to that of the second peak in the V-*L* edge of sXAS spectra.

Sample	Peak area of t_{2g}	Peak area of e_g	Peak area ratio (first/second)
VO_2	0.68786	1.33396	0.5157
TiO_2 (1.7 nm) /VO_2	0.26273	2.43603	0.1079

Sample	FWHM of t_{2g}	FWHM of e_g	FWHM ratio (first/second)
VO_2	1.2036	2.8864	0.4169
TiO_2 (1.7 nm) /VO_2	0.8849	3.9692	0.2229

Supplementary References

1. Z. Zhang, F. Zuo, C. H. Wan, A. Dutta, J. Kim, J. Rensberg, R. Nawrodt, H. H. Park, T. J. Larrabee, X. F. Guan, Y. Zhou, S. M. Prokes, C. Ronning, V. M. Shalaev, A. Boltasseva, M. A. Kats and S. Ramanathan, *Phys. Rev. Appl.*, 2017, **7**, 034008.
2. X. Zhou, X. Yao, X. Qiao, J. Ji, G. Zhou, H. Ji and X. Xu, *Small*, 2025, DOI: https://doi.org/10.1002/smll.202510736, e10736.
3. H. Sim, K.-Y. Doh, Y. Park, K. Song, G.-Y. Kim, J. Son, D. Lee and S.-Y. Choi, *Small*, 2024, **20**, 2402260.
4. Y. Park, H. Sim, K.-Y. Doh, M. Jo, D. Lee, S. Y. Choi and J. Son, *Nano Lett.*, 2022, **22**, 9306-9312.
5. Y. Park, H. Sim, M. Jo, G.-Y. Kim, D. Yoon, H. Han, Y. Kim, K. Song, D. Lee, S.-Y. Choi and J. Son, *Nat. Commun.*, 2020, **11**, 1401.
6. J. Park, H. Yoon, H. Sim, S. Y. Choi and J. Son, *ACS Nano*, 2020, **14**, 2533-2541.
7. X. Zhou, X. Yao, W. Lu, J. Guo, J. Ji, L. Lang, G. Zhou, C. Yao, X. Qiao, H. Ji, Z. Yuan and X. Xu, *Adv. Sci.*, 2025, DOI: https://doi.org/10.1002/advs.202510771, e10771.
8. A. Pofelski, H. Jia, S. Deng, H. Yu, T. J. Park, S. Manna, M. K. Y. Chan, S. K. R. S. Sankaranarayanan, S. Ramanathan and Y. Zhu, *Nano Lett.*, 2024, **24**, 1974-1980.
9. B. Li, M. Hu, H. Ren, C. Hu, L. Li, G. Zhang, J. Jiang and C. Zou, *J. Phys. Chem. Lett.*, 2020, **11**, 10045-10051.
10. S. Chen, Z. Wang, H. Ren, Y. Chen, W. Yan, C. Wang, B. Li, J. Jiang and C. Zou, *Sci. Adv.*, 2019, **5**, eaav6815.
11. Y. L. Chen, Z. W. Wang, S. Chen, H. Ren, L. X. Wang, G. B. Zhang, Y. L. Lu, J. Jiang, C. W. Zou and Y. Luo, *Nat. Commun.*, 2018, **9**, 818.